

# Gelatin-derived sustainable carbon-based functional materials for energy conversion and storage with controllability of structure and component

Zhong-Li Wang,<sup>1</sup> Dan Xu,<sup>1</sup> Hai-Xia Zhong,<sup>1,2</sup> Jun Wang,<sup>1,2</sup> Fan-Lu Meng,<sup>1</sup> Xin-Bo Zhang<sup>1\*</sup>

2015 © The Authors, some rights reserved; exclusive licensee American Association for the Advancement of Science. Distributed under a Creative Commons Attribution Non-Commercial License 4.0 (CC BY-NC). 10.1126/sciadv.1400035

Nonprecious carbon catalysts and electrodes are vital components in energy conversion and storage systems. Despite recent progress, controllable synthesis of carbon functional materials is still a great challenge. We report a novel strategy to prepare simultaneously Fe-N-C catalysts and Fe<sub>3</sub>O<sub>4</sub>/N-doped carbon hybrids based on the sol-gel chemistry of gelatin and iron with controllability of structure and component. The catalysts demonstrate higher catalytic activity and better durability for oxygen reduction than precious Pt/C catalysts. The active sites of FeN<sub>4</sub>/C (D1) and N-FeN<sub>2+2</sub>/C (D3) are identified by Mössbauer spectroscopy, and most of the Fe ions are converted into D1 or D3 species. The oxygen reduction reaction (ORR) activity correlates well with the surface area, porosity, and the content of active Fe-N<sub>x</sub>/C (D1 + D3) species. As an anode material for lithium storage, Fe<sub>3</sub>O<sub>4</sub>/carbon hybrids exhibit superior rate capability and excellent cycling performance. The synthetic approach and the proposed mechanism open new avenues for the development of sustainable carbon-based functional materials.

## INTRODUCTION

Increasing energy demands have stimulated intense research on alternative energy conversion and storage systems with high efficiency, low cost, and environmental benignity. In this important field, electrochemistry provides a bridge for efficient inter-transfer of chemical to electrical energy, such as fuel cells, metal-air batteries, and lithium ion batteries (LIBs) (1–4). However, polarization due to the oxygen reduction reaction (ORR) still contributes significantly to the energy efficiency of fuel cells and metal-air batteries because of the exceptionally high O=O bond energy and the sluggish nature of ORR. Pt or its alloys are the best known ORR catalysts, but their applications are limited by the high cost and declining activity (5–8). To overcome this problem, alternative catalysts based on nonprecious metals materials have been actively pursued (9–15). On the other hand, rechargeable LIBs are key devices for electricity storage and supply. The main challenge in this field is achieving high capacity, excellent cycling performance, and rate capability for both anode and cathode materials to meet the growing power supply requirements for a variety of applications, including portable electronics, electric vehicles, and renewable energy storage (16–21).

Carbon-based functional materials represent the most investigated ORR catalysts and electrode materials for the energy conversion and storage because they not only exhibit excellent electrochemical activity but also have other advantages, including low costs, long durability, and environmental friendliness (22–28). Typically, transition metal-coordinating N/C materials are one of the most promising nonprecious metal catalysts (NPMCs) for the ORR. The traditional method for preparing metal-N-C NPMCs involves direct pyrolysis of the mixture of nitrogen, carbon, and transition metal precursors. N-containing polymers are often adopted as nitrogen and carbon sources in the

preparation of non-noble ORR catalysts. For example, polyaniline, polypyrrole, polyacrylonitrile, polydopamine, polydiaminopyridine, polybenzimidazole, and commercial melamine foam have been investigated to construct Fe/Co-N-C catalysts (29–36). However, the physical mixing of polymers and metal salts frequently fails in controlling the uniform distribution of different components because of their bad compatibility, thus leading to the agglomeration of the metal particles and the microstructural inhomogeneity of these NPMCs (33). The interactions between different components determine the intrinsic nature of active sites. A homogeneous polymer/metal system is very crucial for preparation of high-performance metal-N-C catalysts and is also vitally important for preparation of carbon/metal oxide composite electrode materials. Although polymers derived from transition metal macrocyclic compounds are effective precursors to alleviate the inhomogeneity, these compounds are generally expensive (37–39), even comparable to Pt/C catalysts, which significantly hinders their scalable production. Therefore, how to realize the homogeneous composite system of polymer and transition metal but limit the cost at the same time remains a challenging task for the catalysts and electrode materials.

In this paper, we demonstrate a novel strategy to construct the homogeneous metal/N-containing polymer composite based on the sol-gel chemistry of sustainable gelatin biomolecule and iron nitrate. Gelatin is an animal derivative composed of various proteins with a high average molecular weight (ca. 50,000 to 80,000), which have an average nitrogen content of 16%. Gelatin is produced by partial hydrolysis of collagens that are generally extracted from the boiled bones and connective tissues of animals (40, 41). It is highly economical because it is a naturally abundant and sustainable resource with a high solubility in polar solvents, and thus could be a promising precursor for nitrogen-doped carbons. Herein, we apply the high compatibility and coordinating capability of carboxyl and amide groups in gelatin with metal ions and realize the uniform distribution of metal particles in the carbon precursor during the sol-gel process. It is well known that the sol-gel process has the potential advantage for achieving homogeneous mixing of the components on

<sup>1</sup>State Key Laboratory of Rare Earth Resource Utilization, Changchun Institute of Applied Chemistry, Chinese Academy of Sciences, Changchun 130022, P. R. China. <sup>2</sup>University of Chinese Academy of Sciences, Beijing 100049, P. R. China.

\*Corresponding author. E-mail: xbzhang@ciac.ac.cn

atomic scale (42–44). Furthermore, the gas template of ammonium nitrate is successfully introduced in the gelatin-metal frameworks without affecting the homogeneity, and it enlarges the surface area of the carbon catalysts nearly six times. Benefiting from the synergistic effect of structure and component, these iron-nitrogen-doped porous carbons display an outstanding catalytic performance toward the ORR in alkaline media, superior to precious platinum-carbon (Pt/C) catalysts. Moreover, these novel catalysts can mediate the ORR process in acidic media with excellent activity comparable with Pt/C. The active sites of FeN<sub>4</sub>/C (D1) and N-FeN<sub>2+2</sub>/C (D3) are identified by Mössbauer spectroscopy, and the relative content of D1 + D3 sites is up to 67.6% in all the Fe species, indicating that most of Fe ions are converted into active sites. It should be noted that this strategy can produce not only highly active Fe-N-C catalysts but also high-performance Fe<sub>3</sub>O<sub>4</sub>/N-doped carbon hybrid electrode materials for LIBs with excellent capacity and rate capabilities. To our knowledge, sustainable development of high-performance Fe-N-C catalysts and iron oxide/carbon hybrid materials from economical metal-gelated gelatin biomolecule with controllability of structure and component has never been reported.

## RESULTS

### Synthesis analysis of carbon-based ORR catalysts from gelatin biomolecule

The overall synthetic procedure for the Fe-N-C catalyst is presented in Fig. 1 and in fig. S1. The precursor solution is first prepared by dissolving gelatin, iron nitrate, and ammonium nitrate (fig. S1A). The obvious interaction between iron cation and gelatin is demonstrated by UV-visible spectroscopy (fig. S2). During the thermal treatment at 80°C for 24 hours, the solvent of water gradually evaporates, and complexed iron ions gradually hydrolyze into amorphous ferric hydroxide, accompanying the decomposition of nitrate ions and a big volume expansion as shown in fig. S1B. The mass of final gel is found to equal the total mass of gelatin, ferric hydroxide, and ammonium nitrate, which indicates that ammonium nitrate does not change during the sol-gel process and that it uniformly dispersed in the composite gel with the evaporation of water (fig. S3). In the comparable experiments, it is found that the introduction of iron nitrate in the gelatin

solution is the crucial premise for the sol-gel process owing to the interaction between metal ions and gelatin (figs. S4 to S6). After high-temperature treatment, the homogeneous composite gel is converted into Fe-N-C catalyst with homogeneous distribution of nitrogen, iron, and carbon. A large amount of micropores and mesopores are produced during the decomposition of ammonium nitrate, leading to a high surface area of Fe-N-C catalyst (fig. S7).

### Morphology and structure analysis of carbon-based ORR catalysts

For Fe-N-C catalyst, Fe<sub>3</sub>O<sub>4</sub>/carbon composite is the intermediate product as shown in Fig. 2A. It can be seen that Fe<sub>3</sub>O<sub>4</sub> nanoparticles are uniformly dispersed in the N-doped carbon matrix, identifying the homogeneity of the components. After leaching the iron oxide particles, foam structure can be observed with the formation of large amounts of pores (Fig. 2B). Therefore, iron oxide not only provides iron resource for the Fe-N-C active sites but also acts as a second template for producing porous structure. From the high-resolution transmission electron microscopy (TEM) image of Fig. 2C, dense micropores in the carbon matrix can be clearly observed because of the release of gas template, which provides large catalytic active area. As a comparison, four types of samples are prepared with different precursor components under the same conditions (IAG-C: iron nitrate, ammonium nitrate, and gelatin; AG-C: ammonium nitrate and gelatin; IG-C: iron nitrate and gelatin; and G-C: pure gelatin). From the TEM images of fig. S8, it can be observed that the later three samples have different porous structures compared to IAG-C. Without iron nitrate and ammonium nitrate, the N-doped carbon from pure gelatin has almost no porous structure. In contrast, with addition of iron nitrate or ammonium nitrate, both the samples of AG-C and IG-C have a large amount of micropores. Figure 2D shows the N<sub>2</sub> adsorption-desorption curves of four samples. The surface areas are 1215.4, 725.3, 598.8, and 189.8 m<sup>2</sup> g<sup>-1</sup> for samples IAG-C, AG-C, IG-C, and G-C (table S1), respectively, which is in accordance with the microstructure as discussed above. With the ammonium nitrate as template, the samples IAG-C and AG-C have two kinds of pores: mesopores (4 nm) and micropores (<2 nm), whereas with iron nitrate as template, there is only the micropores produced for IG-C, indicating different component plays different roles (fig. S8D). Therefore, proper combination of iron nitrate and ammonium nitrate

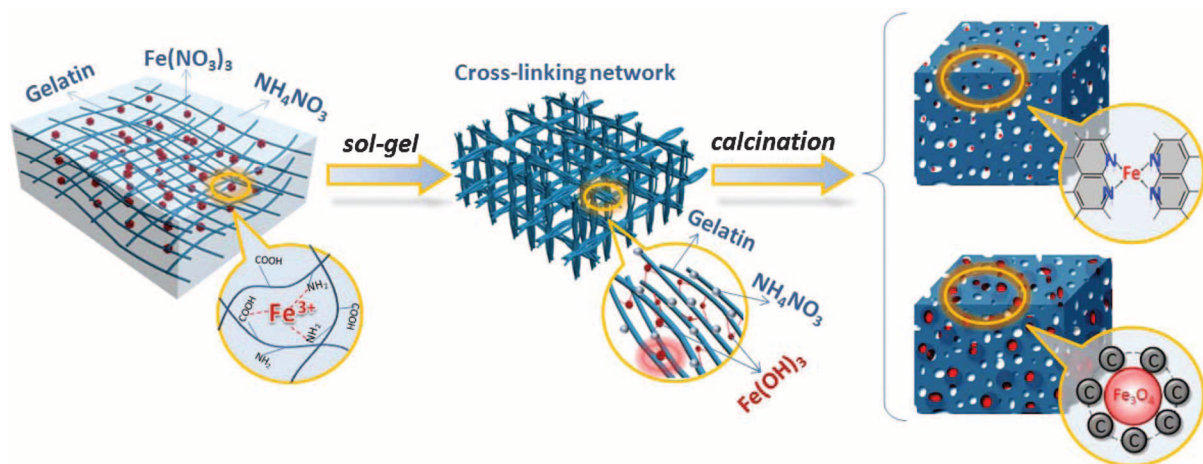
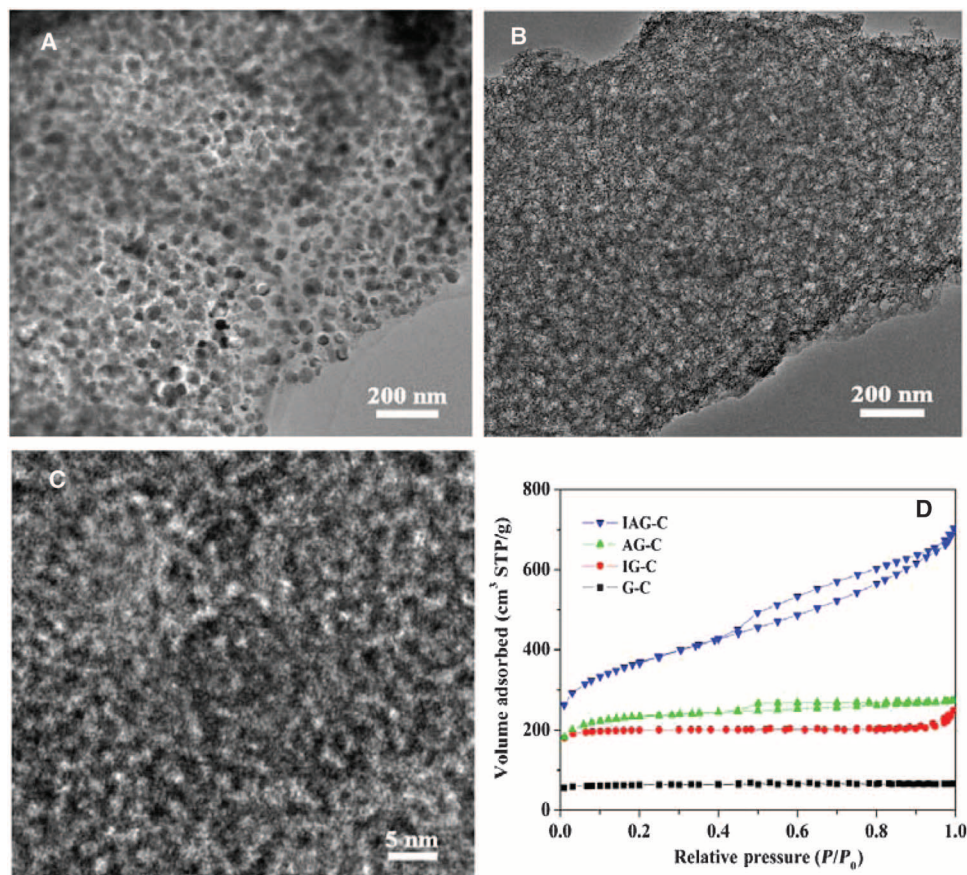


Fig. 1. Illustration of the preparation procedure of IAG-C catalysts and Fe<sub>3</sub>O<sub>4</sub>@AGC electrode materials.



**Fig. 2.** (A) TEM image of intermediate Fe<sub>3</sub>O<sub>4</sub>/carbon composite produced at 350°C. (B and C) TEM and HRTEM images of IAG-C catalyst. (D) Nitrogen adsorption-desorption curves of four samples prepared with different precursors.

has the synergetic effect on producing such high surface area and hierarchical porous structure. Raman spectra and x-ray diffraction (XRD) patterns indicate that the amorphous and defect carbon structure increases with the increase of the surface area from samples G-C to IAG-C (fig. S9).

### Electrochemical properties of carbon-based ORR catalysts

The electrocatalytic activity of prepared carbons is first evaluated by cyclic voltammetry (CV). The onset potential of IAG-C is 1.04 V versus reversible hydrogen electrode (RHE) in O<sub>2</sub>-saturated 0.1 M KOH solution, which is 30 mV more positive than that of commercial Pt/C (Fig. 3A). The IAG-C also exhibits a marked oxygen reduction peak at 0.89 V, superior to Pt/C. In the rotating disk electrode (RDE) experiments (Fig. 3B), the onset potentials of IAG-C and Pt/C are similar at around 1.02 V, close to that identified from CV measurement, but IAG-C exhibits a higher current density and a more positive half-wave potential, indicating more active performance than Pt/C. To gain insight into the production of such high activity, we carried out comparable measurements for samples AG-C, IG-C, and G-C. As shown in Fig. 3B, G-C has no obvious ORR current until a very high overpotential is applied, whereas for AG-C, the high ORR onset potential and a well-defined diffusion-limited current can be observed, which implies that adding ammonium nitrate in the gel to increase the surface area can greatly

enhance the activity. The introduction of Fe ions into the gelatin for sample IG-C results in superior efficiency compared to sample AG-C, even the latter has a higher surface area than the former, indicating that the formation of Fe-N<sub>x</sub> active sites plays more important roles (45). When combining the two advantages in one sample (IAG-C), the ORR activity is greatly enhanced owing to the synergetic effect of large surface area, hierarchical porous structure, and highly active components. The sample IAG-C exhibits super advantages compared to other non-noble catalysts (table S2). The effect of carbonization temperature on the catalytic activity is also investigated, and Fe-N-C catalyst obtained at 900°C is demonstrated to show the highest activity (fig. S10A). To assess the role of iron, the ORR is measured in cyanide ion (CN<sup>-</sup>)-containing KOH electrolyte. The half-wave potential of the catalyst is found to decrease significantly by 108 mV with the decrease of diffusion-limiting current, suggesting the formation of Fe-N<sub>x</sub> complexes (fig. S11A). After thoroughly washing the catalysts to remove bound CN<sup>-</sup>, the as-prepared Fe-N-C catalysts can recover most of its lost current, showing the similar ORR activity as before CN<sup>-</sup> poisoning (fig. S11B), which indicates that the catalytically active sites may be iron macrocycle complexes, such as semimacrocylic-like and macrocylic structures (46, 47).

The four-electron selectivity of as-prepared catalysts and Pt/C is investigated by Koutecky-Levich (K-L) plots at several potentials. The K-L plots of IAG-C (Fig. 3C) show good linearity at all potentials and the electron transfer number *n* is ca. 3.9 to 4.0 even under high potential similar to that of the Pt/C, suggesting that the ORR of IAG-C follows a direct four-electron route. In contrast, the *n* is only around 2 for G-C (fig. S10B). The H<sub>2</sub>O<sub>2</sub> yield from the rotating ring-disk electrode (RRDE) measurements is below 10% for IAG-C in the potential range of 0.15 to 0.85 V, and the corresponding electron transfer number is similar as those derived from K-L plots (fig. S12). The outstanding ORR catalytic activity of IAG-C is further confirmed by the smaller Tafel slope of 58 mV per decade at low overpotentials compared with that of Pt/C (63 mV per decade, Fig. 3D). Under the same mass of catalysts (0.3 mg cm<sup>-2</sup>), the exchange current density (*J*<sub>0</sub>) is obtained from the linear region of the Tafel plot by extrapolating the line (48). The calculated *J*<sub>0</sub> for IAG-C and Pt/C is 1.5 × 10<sup>-8</sup> and 1.3 × 10<sup>-8</sup> A cm<sup>-2</sup>, respectively, further reflecting the excellent activity of as-prepared Fe-N-C catalysts. For the crossover effect of methanol, Pt/C exhibits a marked current decrease immediately after the injection of methanol, indicating the occurrence of methanol oxidation reaction, whereas no noticeable change is observed in the ORR current for IAG-C (Fig. 3E). The results demonstrate that IAG-C has considerably better tolerance to methanol crossover than does Pt/C. Stability is another important aspect of fuel

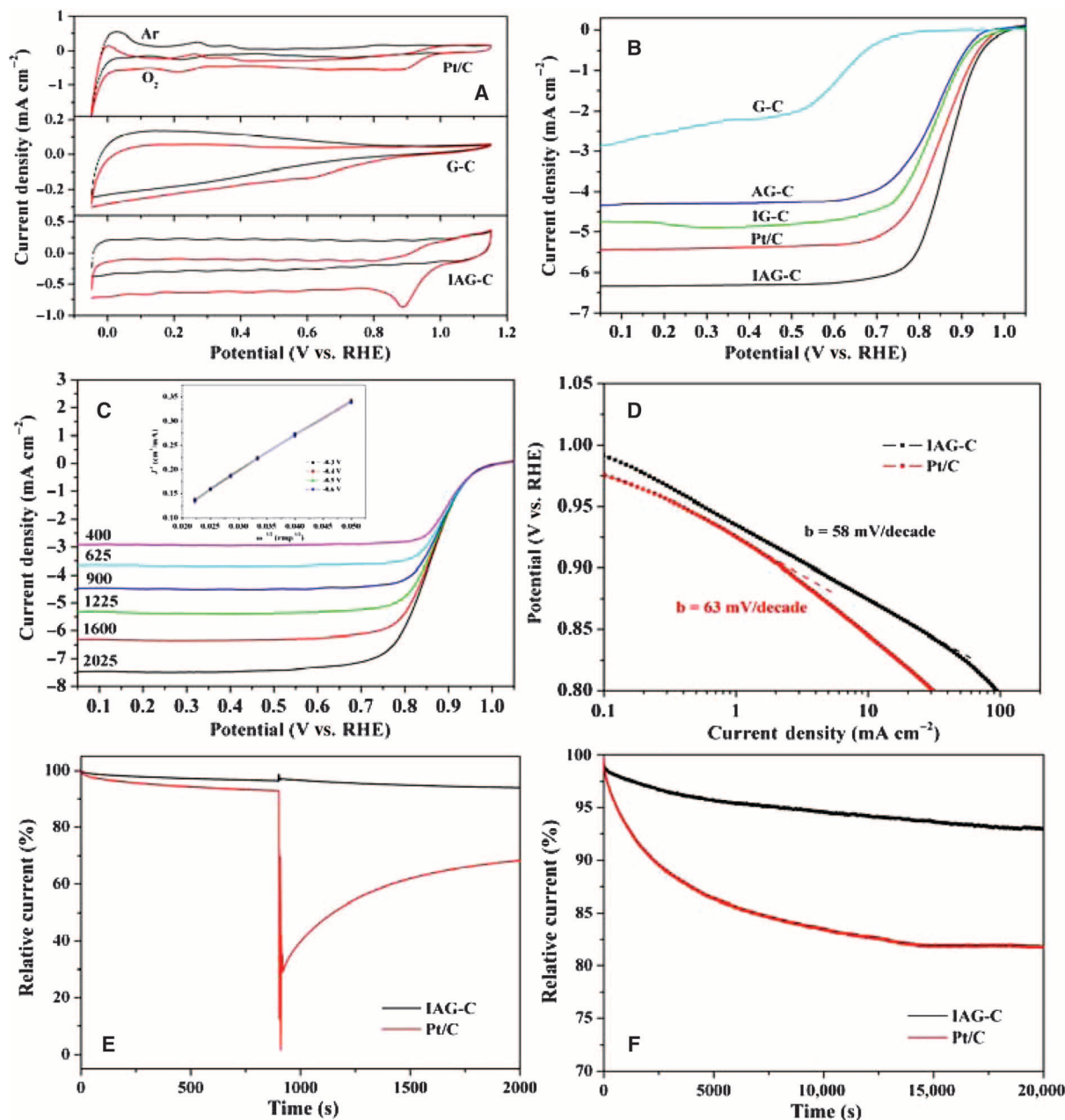


**Fig. 3.** (A) CVs of Pt/C, G-C, and IAG-C in 0.1 M KOH at  $5 \text{ mV s}^{-1}$ . (B) LSV curves for G-C, AG-C, IG-C, IAG-C, and Pt/C in  $\text{O}_2$ -saturated 0.1 M KOH at  $5 \text{ mV s}^{-1}$  at 1600 revolutions per minute (rpm). (C) LSV curves for IAG-C at different rotation rates in  $\text{O}_2$ -saturated 0.1 M KOH at  $5 \text{ mV s}^{-1}$ ; inset shows the K-L plots. (D) Tafel plots of IAG-C and Pt/C for ORR derived

by the mass-transport correction of corresponding RDE data. (E) Chronoamperometric response of IAG-C and Pt/C in  $\text{O}_2$ -saturated 0.1 M KOH followed by addition of 3 M methanol. (F) Chronoamperometric response of IAG-C and Pt/C in  $\text{O}_2$ -saturated 0.1 M KOH solution at 0.65 V at 1600 rpm.

cell catalysts that needs consideration. The chronoamperometric measurements of IAG-C at a constant voltage of 0.65 V displayed only a 7% decrease of current density over 20,000 s, whereas the current of Pt/C decreased by 19% during the same operation (Fig. 3F). This catalyst still keeps high activity after 3 months in air (fig. S10C). Besides being active in alkaline medium, IAG-C catalyst is also found to be an effective ORR catalyst in acidic media with 4e selectivity and, at the same time, shows a much better stability than the Pt/C electrode (figs. S13 and S14).

### Unraveling the correlations of structure-component-activity

To clarify the origin of the enhanced ORR performance of gelatin-derived Fe-N-C catalysts, we characterize the samples by x-ray photoelectron spectroscopy (XPS) and  $^{57}\text{Fe}$  Mössbauer spectroscopy. The nitrogen content of the four samples is very close, in the range of 3.6 to 4.3 at% (table S1). Inductively coupled plasma optical emission spectrometry reveals an iron content of 0.12 to 0.14 at% in the final products. The high-resolution N1s spectra of all catalysts are fitted

with two different signals having binding energies of 398.7 and 400.9 eV, corresponding to pyridinic N and graphitic N (Fig. 4A), respectively, which are generally believed to participate in the active sites (33). The relative content of pyridinic N gradually increases from G-C to IAG-C, whereas that of the graphitic N decreases (Fig. 4B). The large surface area and rich porosity for IAG-C lead to more exposed edge sides with pyridinic N than that for G-C, which will facilitate the formation of co-

ordinating Fe-N active sites (45). Elemental mapping is used to confirm the elemental distribution in the Fe-N-C sample (fig. S15). Uniform distributions of C, N, and Fe throughout the whole sample of IAG-C are detected in the mapping analysis. After stability test, the elemental distribution is still similar to the initial state (fig. S16), and the content of Fe ions remains almost unchanged, reflecting the stability of chemical structure in IAG-C catalyst.

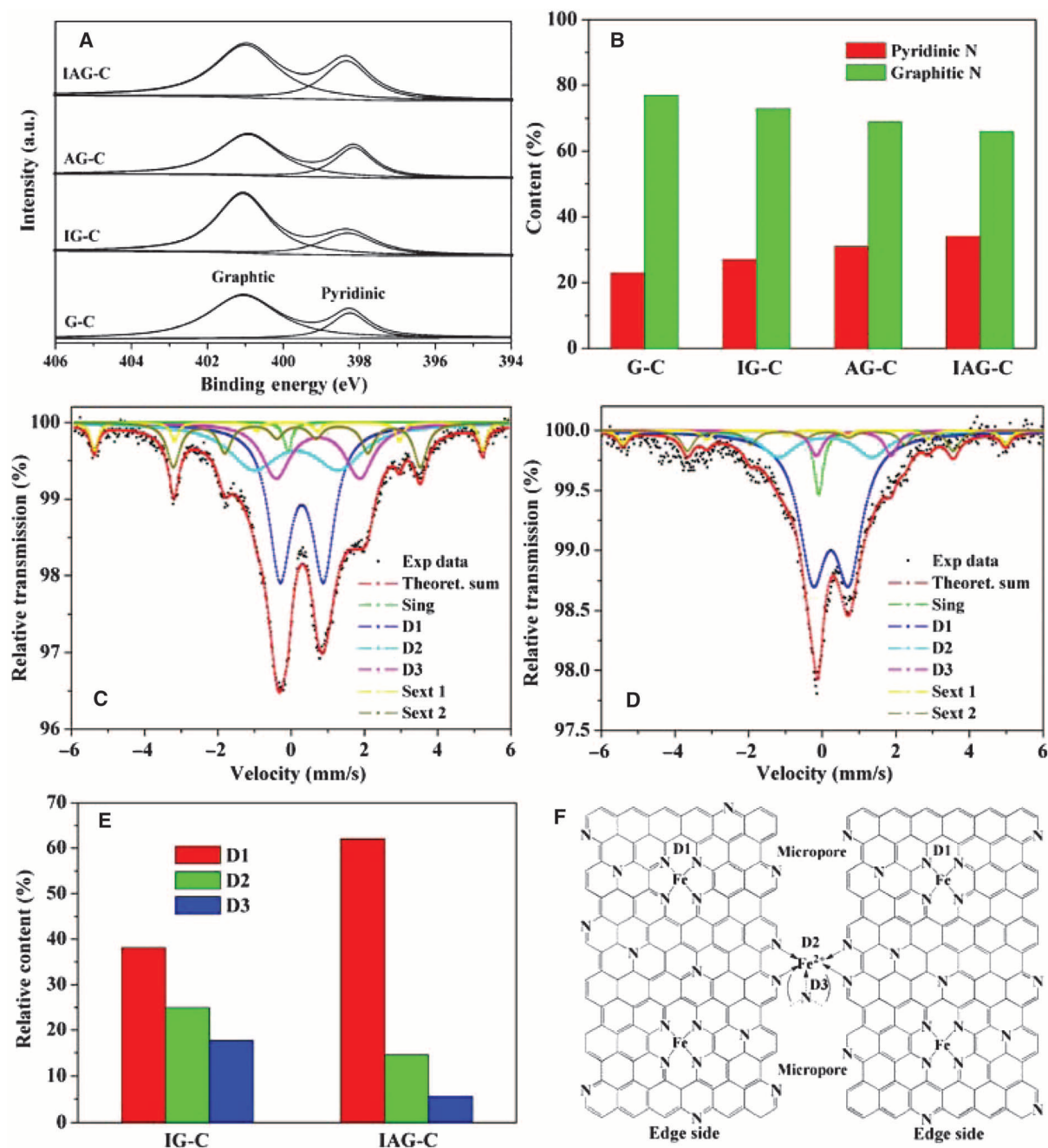


**Fig. 4.** (A and B) N 1s XPS spectra (A) and the relative content of pyridinic and graphitic N (B) in the four samples prepared with different precursors. (C and D) Mössbauer spectra for IG-C and IAG-C. (E) Relative content of D1, D2, and D3 sites in all the Fe species for both Fe-containing catalysts. (F) Possible structure model of IAG-C.

$^{57}\text{Fe}$  Mössbauer spectroscopy is a sensitive tool for characterizing iron-containing compounds and can be used to correlate the ORR activity with the amount of  $\text{Fe-N}_x$  centers (49–51). The Mössbauer spectra of IG-C and IAG-C are shown in Fig. 4, C and D. The spectra can be fitted with singlet, doublet, and sextet lines. Table S3 lists their assignments, with the proportions of different Fe species according to the peak areas. Except for little inactive superparamagnetic iron,  $\alpha\text{-Fe}$ , and iron carbide, most species in the Mössbauer spectra correspond to the three doublets assigned to molecular  $\text{FeN}_4$ -like sites with their ferrous ions in low (D1), intermediate (D2), or high (D3) spin states. As well known, D1 sites with  $S = 0$  and an empty  $3d_z^2$  orbital and D3 sites with  $S = 2$  and a  $3d_z^2$  orbital occupied by a single electron are able to bind oxygen to their  $\text{Fe}^{\text{II}}$  ions in the end-on adsorption mode, which initiates the reduction of oxygen (50). In contrast, D2 sites with the intermediate spin state ( $S = 1$ ) and a completely filled  $3d_z^2$  orbital prevent the end-on adsorption of molecular oxygen, leading to the lack of ORR-activity. From the spectra, it can be seen that the iron species are similar for both catalysts, but their relative contents are different (Fig. 4E). As expected, the sample IAG-C has a much higher content (67.6%) of D1 + D3 active sites compared to IG-C with the content of 55.8%, in accordance with their different ORR activity. This result is also consistent with XPS analysis that the larger surface area and porosity for IAG-C produce more exposed edge-side pyridinic N ligands, which then leads to more active  $\text{Fe-N}_4/\text{C}$  sites. On the basis of all the analysis, the possible structure model of IAG-C is proposed in Fig. 4F.

### Lithium storage performance of iron oxide–carbon hybrids

Besides the highly active  $\text{Fe-N-C}$  catalysts, the sol-gel strategy of gelatin can also produce excellent  $\text{Fe}_3\text{O}_4/\text{N}$ -doped carbon hybrids for LIBs. Figure 5A shows the as-prepared  $\text{Fe}_3\text{O}_4/\text{N}$ -doped carbon hybrid ( $\text{Fe}_3\text{O}_4@\text{AGC}$ ) from the composite gel after high-temperature treatment. It can be observed that  $\text{Fe}_3\text{O}_4$  nanoparticles are uniformly confined in three-dimensional frameworks. The high-resolution TEM image in Fig. 5B shows the interfacial structure between carbon matrix and the  $\text{Fe}_3\text{O}_4$  particle. Thermogravimetric analysis of  $\text{Fe}_3\text{O}_4@\text{AGC}$  reveals that the weight fraction of  $\text{Fe}_3\text{O}_4$  in the composites is 78%. It is noted that, keeping the hybrid structure, the content of  $\text{Fe}_3\text{O}_4$  can be variable from 70 to 94% by adjusting the ratio of metal salt and gelatin as shown in figs. S17 and S18. As anode materials of LIBs,  $\text{Fe}_3\text{O}_4@\text{AGC}$  manifests an exceptionally high rate capability compared with bare  $\text{Fe}_3\text{O}_4$  (Fig. 5C). For example, at a current density of  $5000 \text{ mA g}^{-1}$ ,  $\text{Fe}_3\text{O}_4@\text{AGC}$  still delivers a favorable capacity of  $260 \text{ mAh g}^{-1}$ , whereas bare  $\text{Fe}_3\text{O}_4$  only exhibits a capacity of  $45 \text{ mAh g}^{-1}$ . Moreover, when the current rate is returned to  $100 \text{ mA g}^{-1}$ , the stable high capacity of  $\text{Fe}_3\text{O}_4@\text{AGC}$  ( $820 \text{ mAh g}^{-1}$ ) is resumed. Except for the rate capability, the cycling performance

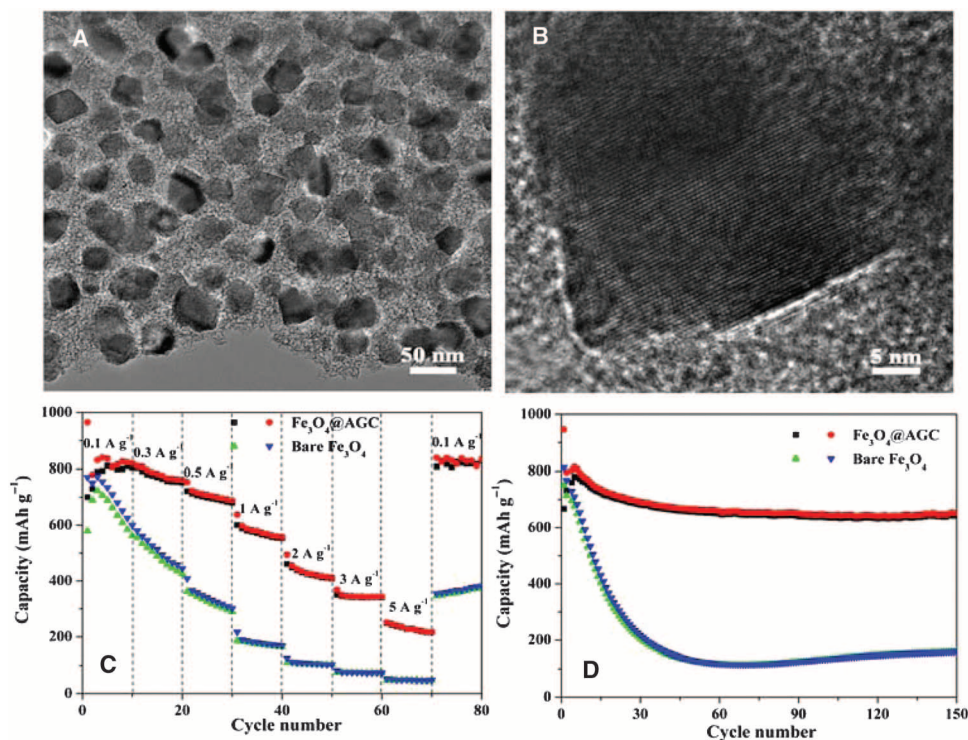


**Fig. 5.** (A and B) TEM (A) and HRTEM (B) images of  $\text{Fe}_3\text{O}_4@\text{AGC}$  electrode material. (C and D) Comparison of rate capabilities (C) and cycle performance (D) of  $\text{Fe}_3\text{O}_4@\text{AGC}$  and bare  $\text{Fe}_3\text{O}_4$ .

of  $\text{Fe}_3\text{O}_4@\text{AGC}$  is also superior to that of bare  $\text{Fe}_3\text{O}_4$  particles (Fig. 5D). Although the initial capacities of both samples are similar, the gap of retentions is great. After 150 cycles at  $500 \text{ mA g}^{-1}$ , the capacity of  $\text{Fe}_3\text{O}_4@\text{AGC}$  ( $660 \text{ mAh g}^{-1}$ ) is four times more than that of bare  $\text{Fe}_3\text{O}_4$  particles ( $150 \text{ mAh g}^{-1}$ ). Although the performance of  $\text{Fe}_3\text{O}_4@\text{AGC}$  is similar to that of complex  $\text{Fe}_3\text{O}_4/\text{graphene}$  composites (18, 20, 52), the preparation method of the former is more facile and sustainable than that of the latter, which makes  $\text{Fe}_3\text{O}_4@\text{AGC}$  more favorable for large-scale applications.

### DISCUSSION

In summary, we have reported a novel strategy to simultaneously prepare nonprecious  $\text{Fe-N-C}$  catalysts and  $\text{Fe}_3\text{O}_4/\text{N}$ -doped carbon hybrids on the basis of the sol-gel chemistry of economical gelatin and iron. The surface area, porosity, and active component can be controlled by different precursors and treatments. After optimization of structure, most of Fe ions are converted into active  $\text{Fe-N}_4/\text{C}$  species. The  $\text{Fe-N-C}$  catalysts exhibit a more positive half-wave potential, a high and stable limiting current, excellent stability for oxygen reduction compared to precious  $\text{Pt/C}$  catalysts. As anode materials for LIBs,  $\text{Fe}_3\text{O}_4/\text{carbon}$  hybrids solve the structural integrity and electrical conductivity of pure  $\text{Fe}_3\text{O}_4$  and greatly improve the rate capability and cycling performance. The synthetic approach and the proposed mechanism open new avenues for the sustainable development of carbon-based catalysts and electrode materials for fuel cells, batteries, supercapacitors, and other energy conversion and storage systems.

## MATERIALS AND METHODS

## Synthesis of catalysts and electrode materials

In a typical process, 1.616 g of  $\text{Fe}(\text{NO}_3)_3 \cdot 9\text{H}_2\text{O}$  (4 mmol) and 3.6 g of  $\text{NH}_4\text{NO}_3$  were dissolved in 20 ml of  $\text{H}_2\text{O}$ , and then 2 g of gelatin was added under stirring at  $80^\circ\text{C}$ . When the gelatin was dissolved completely, the formed scarlet and viscous precursor solution was poured into the evaporating dish. After gelation at  $80^\circ\text{C}$  for 24 hours, dry xerogel was obtained and used as common raw material for catalysts and electrode materials. For the synthesis of catalysts, the xerogel was first calcined in  $\text{N}_2$  at  $350^\circ\text{C}$  for 2 hours and then washed with 1 M HCl. Subsequently, the product was calcined at  $900^\circ\text{C}$  for 2 hours in  $\text{N}_2$  and washed again with 0.1 M HCl. The final product was obtained after a second heat treatment at  $900^\circ\text{C}$  in  $\text{N}_2$ . For comparison, four types of samples were prepared with different precursor components under the same conditions (sample IAG-C: iron nitrate, ammonium nitrate, and gelatin; sample IG-C: iron nitrate and gelatin; sample AG-C: ammonium nitrate and gelatin; and sample G-C: pure gelatin). For AG-C and G-C, second heat treatment was not necessary because of the absence of iron.

The synthesis of electrode materials was relatively simple. The  $\text{Fe}_3\text{O}_4/\text{N}$ -doped carbon hybrid was obtained by calcining the xerogel in  $\text{N}_2$  at  $650^\circ\text{C}$  for 2 hours. The content of  $\text{Fe}_3\text{O}_4$  in the hybrid could be adjusted by varying the amount of  $\text{Fe}(\text{NO}_3)_3 \cdot 9\text{H}_2\text{O}$ . The amount of 2.02 g (5 mmol) corresponds to the sample of  $\text{Fe}_3\text{O}_4/\text{AGC}$ , and the amounts of 1.616 g (4 mmol) and 2.424 g (6 mmol) correspond to  $\text{Fe}_3\text{O}_4/\text{AGC-4}$  and  $\text{Fe}_3\text{O}_4/\text{AGC-6}$ , respectively.

## Electrocatalysis measurements

Electrochemical characterizations were performed on a VMP3 electrochemical workstation (Bio-Logic Inc.) with a three-electrode system. A glassy carbon electrode of 5.6 mm in diameter was used as the working electrode, a Pt foil as the counter electrode, and a saturated Ag/AgCl electrode as the reference electrode. For electrode preparation, 5 mg of sample catalyst and 30  $\mu\text{l}$  of Nafion (5 wt %) solution were first homogeneously dispersed in 1 ml of 2:1 (v/v) water/isopropanol mixed solvent by sonication for at least 30 min. Next, 15  $\mu\text{l}$  of the catalyst ink was loaded onto the glassy carbon electrode. Commercial Pt/C (20% platinum supported on Vulcan XC-72R carbon from Johnson Matthey) electrode was prepared by the same procedure. Catalyst loading for all samples, including Pt/C, was  $0.3 \text{ mg cm}^{-2}$ . KOH (0.1 M) was saturated with  $\text{O}_2$  by bubbling oxygen for 20 min before testing. For CV measurements, the working electrode was cycled between  $-1.0$  and  $0.2 \text{ V}$  at a scan rate of  $100\text{--}5 \text{ mV s}^{-1}$  with continuous  $\text{O}_2$  flow. For control experiments in Ar-saturated KOH, switching  $\text{O}_2$  to Ar and the other procedures remain unchanged. RDE measurements were conducted at different rotating speeds from 400 to 2025 rpm at a scan rate of  $5 \text{ mV s}^{-1}$ . K-L plots were analyzed at various potentials to determine the number of electrons transferred based on the K-L equation:

$$\frac{1}{J} = \frac{1}{J_L} + \frac{1}{J_K} = \frac{1}{B\omega^{1/2}} + \frac{1}{J_K}$$

$$B = 0.20nFC_0D_0^{2/3}\nu^{-1/6}$$

where  $J$  and  $J_K$  are the measured and kinetic-limiting current densities,  $\omega$  is the rotation speed,  $n$  is transferred electron number,  $F$  is the Faraday constant ( $F = 96485 \text{ C mol}^{-1}$ ),  $D_0$  is the diffusion coefficient

of  $\text{O}_2$  ( $1.9 \times 10^{-5} \text{ cm}^2 \text{ s}^{-1}$ ),  $\nu$  is the kinematic viscosity ( $\nu = 0.01 \text{ cm}^2 \text{ s}^{-1}$ ), and  $C_0$  is the concentration of  $\text{O}_2$  in the solution ( $1.2 \times 10^{-6} \text{ mol cm}^{-3}$ ). The constant 0.2 is adopted when rotation speed is expressed in rpm. For the RRDE test, the disk potential was scanned at  $5 \text{ mV s}^{-1}$ , whereas the ring electrode was held at 1.2 V versus RHE. All the ORR currents presented in the figures are Faradaic currents, that is, after correction for the capacitive current. For Tafel plots, the kinetic current was determined after mass-transport correction of RDE curves by

$$J_K = \frac{J \times J_L}{J_L - J}$$

The following equations were used to calculate  $n$  (the apparent number of electrons transferred during ORR) and % $\text{H}_2\text{O}_2$  (the percentage of  $\text{H}_2\text{O}_2$  released during ORR):

$$n = \frac{4I_D}{I_D + (I_R/N)}$$

$$\% \text{H}_2\text{O}_2 = 200 \times \frac{I_R/N}{I_D + (I_R/N)}$$

## Lithium storage measurement

The positive electrodes were fabricated by mixing 80 wt % active materials, 10 wt % acetylene black, and 10 wt % polyvinylidene difluoride binder in appropriate amount of NMP as solvent. Then the resulting paste was spread on a Cu foil by Automatic Film Coater with Vacuum Pump & Micrometer Doctor Blade (MTI). After the NMP solvent evaporation in a vacuum oven at  $120^\circ\text{C}$  for 12 hours, the electrodes were pressed and cut into disks. A CR2032 coin-type cell was assembled with lithium metal as the counter and reference electrode and polypropylene film as a separator. The cells were constructed and handled in an argon-filled glovebox. The charge-discharge measurements were carried out using the Land battery system (CT2001A) at a constant current density in a voltage range of 0.01 to 3 V versus  $\text{Li}/\text{Li}^+$ . The capacity is based on the total mass of hybrid.

## SUPPLEMENTARY MATERIALS

Supplementary material for this article is available at <http://advances.sciencemag.org/cgi/content/full/1/1/e1400035/DC1>

## Materials and Methods

- Fig. S1. Photographs of precursor solution (A), composite gel (B), and the final catalyst (C).  
 Fig. S2. Comparison of photographs and UV-visible spectroscopy of different solutions.  
 Fig. S3. (A) SEM image of composite gel after sol-gel; (B to E) mapping analysis of the composite gel: (B) C element from gelatin, (C) N and (D) O elements from gelatin and ammonium nitrate, and (E) Fe element from iron ferric hydroxide.  
 Fig. S4. Comparison of the products derived from different precursor solution containing different components at the same treatment conditions: (A) only gelatin; (B) gelatin and ammonium nitrate; and (C) gelatin and iron nitrate.  
 Fig. S5. Comparison of gels obtained by using cobalt nitrate (A) and nickel nitrate (B) as metal salts with the same treatment conditions of iron nitrate.  
 Fig. S6. (A) FT-IR spectra, (B) N 1s spectra, and (C) XRD patterns of gelatin, amorphous  $\text{Fe}(\text{OH})_3$ , and gelatin- $\text{Fe}(\text{OH})_3$  gel.  
 Fig. S7. (A) SEM image of composite gel after sol-gel; (B) SEM image and (C) XRD pattern of the product obtained by calcining the gel at  $350^\circ\text{C}$ ; (D) TEM image of the above HCl-washed product.  
 Fig. S8. TEM images of AG-C (A), IG-C (B), and G-C (C); (D) pore size distributions of four samples prepared with different precursors.  
 Fig. S9. Raman spectra (A) and  $I_D/I_G$  ratio (B) of four samples prepared with different precursors. (C) Comparison of XRD patterns of IAG-C and G-C.  
 Fig. S10. (A) Temperature effect of IAG-C activity for ORR; (B) comparison of the electron transfer number of catalysts at 0.65 V; (C) stability of IAG-C after 3 months in air.

Fig. S11. LSV curves of IAG-C before and after adding KCN in O<sub>2</sub>-saturated 0.1 M KOH at 1600 rpm: (A) 10 mM KCN and (B) 50 mM KCN. The green line is the LSV curve after CN<sup>-</sup> poisoning tests, electrode washing, and immersion in fresh 0.1 M KOH for IAG-C.

Fig. S12. LSV curves at different rotation rates in O<sub>2</sub>-saturated 0.1 M KOH at 5 mV s<sup>-1</sup>, and the inset shows the corresponding K-L plots: (A) G-C, (B) AG-C, (C) IG-C, and (D) Pt/C; (E) electron transfer number (*n*) and (F) peroxide yield of G-C, AG-C, IG-C, IAG-C, and commercial 20 wt % Pt/C in O<sub>2</sub>-saturated 0.1 M KOH.

Fig. S13. (A) Linear sweep voltammetry (LSV) curves for G-C, AG-C, IG-C, IAG-C, and Pt/C in O<sub>2</sub>-saturated 0.1 M HClO<sub>4</sub> at 5 mV s<sup>-1</sup> at 1600 rpm; LSV curves for IAG-C (B) and Pt/C (C) at different rotation rates in O<sub>2</sub>-saturated 0.1 M HClO<sub>4</sub> at 5 mV s<sup>-1</sup>, and the inset shows the K-L plots.

Fig. S14. (A) Electron transfer number and (B) peroxide yield (*n*) of G-C, AG-C, IG-C, IAG-C, and commercial 20 wt % Pt/C in O<sub>2</sub>-saturated 0.1 M HClO<sub>4</sub>; (C) chronoamperometric response of IAG-C and Pt/C in O<sub>2</sub>-saturated 0.1 M HClO<sub>4</sub> followed by addition of 3 M methanol; (D) chronoamperometric response of IAG-C and Pt/C in O<sub>2</sub>-saturated 0.1 M HClO<sub>4</sub> solution at 0.5 V (versus RHE) at 1600 rpm.

Fig. S15. (A) High-angle annular dark-field scanning transmission electron microscopy (STEM) image of the IAG-C catalyst; (B) C-, (C) N-, (D) O-, and (E) Fe-elemental mapping of the square region.

Fig. S16. (A) High-angle annular dark-field scanning transmission electron microscopy (STEM) image of the IAG-C catalyst; (B) C-, (C) N-, (D) O-, and (E) Fe-elemental mapping of the square region after stability test. (F) N 1s XPS spectra of IAG-C after stability test.

Fig. S17. TEM images of Fe<sub>3</sub>O<sub>4</sub>@AGC with different content of Fe<sub>3</sub>O<sub>4</sub> in the hybrids: (A) Fe<sub>3</sub>O<sub>4</sub>@AGC-4, (B) Fe<sub>3</sub>O<sub>4</sub>@AGC, and (C) Fe<sub>3</sub>O<sub>4</sub>@AGC-6; (D) TG curves of the three hybrids to determine the content of carbon; (E) XRD patterns of three hybrids. The diffraction peaks of the composites are perfectly indexed to pure-phase Fe<sub>3</sub>O<sub>4</sub> (JCPDS No.65-3107).

Fig. S18 Charge-discharge curves of Fe<sub>3</sub>O<sub>4</sub>@AGC (A), bare Fe<sub>3</sub>O<sub>4</sub> (B), and AGC (C) at a current density of 100 mA g<sup>-1</sup>; (D) Nyquist plots for the Fe<sub>3</sub>O<sub>4</sub>@AGC and bare Fe<sub>3</sub>O<sub>4</sub>-based cells with lithium metal as counter electrode.

Fig. S19. The calibration CV curves of Ag/AgCl electrode (A) in 0.1 M KOH and (B) in 0.1 M HClO<sub>4</sub> with respect to RHE.

## REFERENCES AND NOTES

- M. Lefèvre, E. Proietti, F. Jaouen, J. P. Dodelet, Iron-based catalysts with improved oxygen reduction activity in polymer electrolyte fuel cells. *Science* **324**, 71–74 (2009).
- G. Wu, K. L. More, C. M. Johnston, P. Zelenay, High-performance electrocatalysts for oxygen reduction derived from polyaniline, iron, and cobalt. *Science* **332**, 443–447 (2011).
- Y. Y. Liang, Y. G. Li, H. L. Wang, J. G. Zhou, J. Wang, T. Regier, H. J. Dai, Co<sub>3</sub>O<sub>4</sub> nanocrystals on graphene as a synergistic catalyst for oxygen reduction reaction. *Nat. Mater.* **10**, 780–786 (2011).
- Y. G. Li, W. Zhou, H. L. Wang, L. M. Xie, Y. Y. Liang, F. Wei, J. C. Idrobo, S. J. Pennycook, H. J. Dai, An oxygen reduction electrocatalyst based on carbon nanotube-graphene complexes. *Nat. Nanotechnol.* **7**, 394–400 (2012).
- S. Guo, S. Zhang, S. Sun, Tuning nanoparticle catalysis for the oxygen reduction reaction. *Angew. Chem. Int. Ed. Engl.* **52**, 8526–8544 (2013).
- F. Y. Cheng, J. Chen, Metal-air batteries: From oxygen reduction electrochemistry to cathode catalysts. *Chem. Soc. Rev.* **42**, 2172–2192 (2012).
- H. Zhu, S. Zhang, S. J. Guo, D. Su, S. H. Sun, Synthetic control of FePtM nanorods (M = Cu, Ni) to enhance the oxygen reduction reaction. *J. Am. Chem. Soc.* **135**, 7130–7133 (2013).
- S. S. Kocha, J. W. Zack, S. M. Alia, K. C. Neyerlin, B. S. Pivovar, Influence of ink composition on the electrochemical properties of Pt/C electrocatalysts. *ECS Trans.* **50**, 1475–1485 (2012).
- R. Silva, D. Voiry, M. Chhowalla, T. Asefa, Efficient metal-free electrocatalysts for oxygen reduction: Polyaniline-derived N- and O-doped mesoporous carbons. *J. Am. Chem. Soc.* **135**, 7823–7826 (2013).
- Y. Zheng, Y. Jiao, L. Ge, M. Jaroniec, S. Z. Qiao, Two-step boron and nitrogen doping in graphene for enhanced synergistic catalysis. *Angew. Chem. Int. Ed. Engl.* **52**, 3110–3116 (2013).
- Y. Zheng, Y. Jiao, Y. Zhu, L. H. Li, Y. Han, Y. Chen, A. Du, M. Jaroniec, S. Z. Qiao, Hydrogen evolution by a metal-free electrocatalyst. *Nat. Commun.* **5**, 3783 (2014).
- Y. Liang, Y. Li, H. Wang, H. Dai, Strongly coupled inorganic/nanocarbon hybrid materials for advanced electrocatalysis. *J. Am. Chem. Soc.* **135**, 2013–2036 (2013).
- X. Zou, X. Huang, A. Goswami, R. Silva, B. R. Sathe, E. Mikmekova, T. Asefa, Cobalt-embedded nitrogen-rich carbon nanotubes efficiently catalyze hydrogen evolution reaction at all pH values. *Angew. Chem. Int. Ed. Engl.* **53**, 4372–4376 (2014).
- J. He, Y. J. Liu, T. Babu, Z. J. Wei, Z. H. Nie, Self-assembly of inorganic nanoparticle vesicles and tubules driven by tethered linear block copolymers. *J. Am. Chem. Soc.* **134**, 11342–11345 (2012).
- J. He, M. T. Perez, P. Zhang, T. Babu, Y. Liu, J. L. Gong, Z. H. Nie, A general approach to synthesize asymmetric hybrid nanoparticles by interfacial reactions. *J. Am. Chem. Soc.* **134**, 3639–3642 (2012).
- L. Suo, Y. S. Hu, H. Li, M. Armand, L. Chen, A new class of solvent-in-salt electrolyte for high-energy rechargeable metallic lithium batteries. *Nat. Commun.* **4**, 1481 (2013).
- X. Cao, B. Zheng, X. Rui, W. Shi, Q. Yan, H. Zhang, Metal oxide-coated three-dimensional graphene prepared by the use of metal-organic frameworks as precursors. *Angew. Chem. Int. Ed. Engl.* **53**, 1404–1409 (2014).
- W. Wei, S. B. Yang, H. X. Zhou, I. Lieberwirth, X. L. Feng, K. Müllen, 3D graphene foams cross-linked with pre-encapsulated Fe<sub>3</sub>O<sub>4</sub> nanospheres for enhanced lithium storage. *Adv. Mater.* **25**, 2909–2914 (2013).
- E. Kang, Y. S. Jung, A. S. Cavanagh, G. H. Kim, S. M. George, A. C. Dillon, J. K. Kim, J. Lee, Fe<sub>3</sub>O<sub>4</sub> nanoparticles confined in mesocellular carbon foam for high performance anode materials for lithium-ion batteries. *Adv. Funct. Mater.* **21**, 2430–2438 (2011).
- G. M. Zhou, D. W. Wang, F. Li, L. L. Zhang, N. Li, Z. S. Wu, L. Wen, G. Q. (Max) Lu, H. M. Cheng, Graphene-wrapped Fe<sub>3</sub>O<sub>4</sub> anode material with improved reversible capacity and cyclic stability for lithium ion batteries. *Chem. Mater.* **22**, 5306–5313 (2010).
- D. Yang, Z. Lu, X. Rui, X. Huang, H. Li, J. Zhu, W. Zhang, Y. M. Lam, H. H. Hng, H. Zhang, Q. Yan, Synthesis of two-dimensional transition-metal phosphates with highly ordered mesoporous structures for lithium-ion battery applications. *Angew. Chem. Int. Ed. Engl.* **53**, 9352–9355 (2014).
- P. Chen, T. Y. Xiao, Y. H. Qian, S. S. Li, S. H. Yu, A nitrogen-doped graphene/carbon nanotube nanocomposite with synergistically enhanced electrochemical activity. *Adv. Mater.* **25**, 3192–3196 (2013).
- Z. Xiang, D. Cao, L. Huang, J. Shui, M. Wang, L. Dai, Nitrogen-doped holey graphitic carbon from 2D covalent organic polymers for oxygen reduction. *Adv. Mater.* **26**, 3315–3320 (2014).
- W. Wei, H. Liang, K. Parvez, X. Zhuang, X. L. Feng, K. Müllen, Nitrogen-doped carbon nanosheets with size-defined mesopores as highly efficient metal-free catalyst for the oxygen reduction reaction. *Angew. Chem. Int. Ed. Engl.* **126**, 1596–1600 (2014).
- X. Huang, Z. Y. Zeng, H. Zhang, Metal dichalcogenide nanosheets: Preparation, properties and applications. *Chem. Soc. Rev.* **42**, 1934–1946 (2013).
- J. Liu, T. Yang, D. W. Wang, G. Q. (Max) Lu, D. Y. Zhao, S. Z. Qiao, A facile soft-template synthesis of mesoporous polymeric and carbonaceous nanospheres. *Nat. Commun.* **4**, 2798 (2013).
- J. Zhu, D. Yang, Z. Yin, Q. Yan, H. Zhang, Graphene and graphene-based materials for energy storage applications. *Small*, **10**, 3480–3498 (2014).
- X. Huang, X. Qi, F. Boey, H. Zhang, Graphene-based composites. *Chem. Soc. Rev.* **41**, 666–686 (2012).
- Z. Wen, S. Ci, F. Zhang, X. Feng, S. Cui, S. Mao, S. Luo, Z. He, J. Chen, Nitrogen-enriched core-shell structured Fe/Fe<sub>3</sub>C-C nanorods as advanced electrocatalysts for oxygen reduction reaction. *Adv. Mater.* **24**, 1399–1404 (2012).
- Y. Zhao, K. Watanabe, K. Hashimoto, Self-supporting oxygen reduction electrocatalysts made from a nitrogen-rich network polymer. *J. Am. Chem. Soc.* **134**, 19528–19531 (2012).
- J. S. Lee, G. S. Park, S. T. Kim, M. L. Liu, J. Cho, A highly efficient electrocatalyst for the oxygen reduction reaction: N-doped Ketjenblack incorporated into Fe/Fe<sub>3</sub>C-functionalized melamine foam. *Angew. Chem. Int. Ed. Engl.* **52**, 1026–1030 (2013).
- Y. Q. Chang, F. Hong, C. X. He, Q. L. Zhang, J. J. Liu, Nitrogen and sulfur dual-doped non-noble catalyst using fluidic acrylonitrile telomer as precursor for efficient oxygen reduction. *Adv. Mater.* **25**, 4794–4799 (2013).
- H. W. Liang, W. Wei, Z. S. Wu, X. L. Feng, K. Müllen, Mesoporous metal-nitrogen-doped carbon electrocatalysts for highly efficient oxygen reduction reaction. *J. Am. Chem. Soc.* **135**, 16002–16005 (2013).
- D. Zhao, J. L. Shui, L. R. Grabstanowicz, C. Chen, S. M. Commet, T. Xu, J. Lu, D. J. Liu, Highly efficient non-precious metal electrocatalysts prepared from one-pot synthesized zeolitic imidazolate frameworks. *Adv. Mater.* **26**, 1093–1097 (2014).
- E. Proietti, F. Jaouen, M. Lefèvre, N. Larouche, J. Tian, J. Herranz, J. P. Dodelet, Iron-based cathode catalyst with enhanced power density in polymer electrolyte membrane fuel cells. *Nat. Commun.* **2**, 416 (2011).
- H. T. Chung, J. H. Won, P. Zelenay, Active and stable carbon nanotube/nanoparticle composite electrocatalyst for oxygen reduction. *Nat. Commun.* **4**, 1922 (2013).
- S. Yuan, J. L. Shui, L. Grabstanowicz, C. Chen, S. Commet, B. Reprögle, T. Xu, L. Yu, D. J. Liu, A highly active and support-free oxygen reduction catalyst prepared from ultrahigh-surface-area porous polyporphyrin. *Angew. Chem. Int. Ed. Engl.* **52**, 8349–8354 (2013).
- Z. S. Wu, L. Chen, J. Liu, K. Parvez, H. Liang, J. Shu, H. Sachdev, R. Graf, X. Feng, K. Müllen, High-performance electrocatalysts for oxygen reduction derived from cobalt porphyrin-based conjugated mesoporous polymers. *Adv. Mater.* **26**, 1450–1454 (2014).
- Z. H. Xiang, Y. H. Xue, D. P. Cao, L. Huang, J. F. Chen, L. M. Dai, Highly efficient electrocatalysts for oxygen reduction based on 2D covalent organic polymers complexed with non-precious metals. *Angew. Chem. Int. Ed. Engl.* **53**, 2433–2437 (2014).
- G. P. Mane, S. N. Talapaneni, C. Anand, S. Varghese, H. Iwai, Q. Ji, K. Ariga, T. Mori, A. Vinu, Preparation of highly ordered nitrogen-containing mesoporous carbon from a gelatin biomolecule and its excellent sensing of acetic acid. *Adv. Funct. Mater.* **22**, 3596–3604 (2012).



41. G. Nam, J. Park, S. T. Kim, D. B. Shin, N. Park, Y. Kim, J. S. Lee, J. Cho, Metal-free Ketjenblack incorporated nitrogen-doped carbon sheets derived from gelatin as oxygen reduction catalysts. *Nano Lett.* **14**, 1870–1876 (2014).
42. Z. Schnopp, Biopolymers as a flexible resource for nanochemistry. *Angew. Chem. Int. Ed. Engl.* **52**, 1096–1108 (2013).
43. M. Antonietti, N. Fochler, T. P. Fellingner, Carbon aerogels and monoliths: Control of porosity and nanoarchitecture via sol-gel routes. *Chem. Mater.* **26**, 196–210 (2014).
44. H. R. Yue, Y. J. Zhao, S. Zhao, B. Wang, X. B. Ma, J. L. Gong, A copper-phyllsilicate core-sheath nanoreactor for carbon-oxygen hydrogenolysis reactions. *Nat. Commun.* **4**, 2339 (2013).
45. N. Ramaswamy, U. Tylus, Q. Jia, S. Mukerjee, Activity descriptor identification for oxygen reduction on nonprecious electrocatalysts: Linking surface science to coordination chemistry. *J. Am. Chem. Soc.* **135**, 15443–15449 (2013).
46. W. Li, A. Yu, D. C. Higgins, B. G. Llanos, Z. W. Chen, Biologically inspired highly durable iron phthalocyanine catalysts for oxygen reduction reaction in polymer electrolyte membrane fuel cells. *J. Am. Chem. Soc.* **132**, 17056–17058 (2010).
47. W. Li, J. Wu, D. C. Higgins, J. Y. Choi, Z. W. Chen, Determination of iron active sites in pyrolyzed iron-based catalysts for the oxygen reduction reaction. *ACS Catal.* **2**, 2761–2768 (2012).
48. Y. Jiao, Y. Zheng, M. Jaroniec, S. Z. Qiao, Origin of the electrocatalytic oxygen reduction activity of graphene-based catalysts: A roadmap to achieve the best performance. *J. Am. Chem. Soc.* **136**, 4394–4403 (2014).
49. U. I. Kramm, M. Lefèvre, N. Larouche, D. Schmeisser, J. P. Dodelet, Correlations between mass activity and physicochemical properties of Fe/N/C catalysts for the ORR in PEM fuel cell via  $^{57}\text{Fe}$  Mössbauer spectroscopy and other techniques. *J. Am. Chem. Soc.* **136**, 978–985 (2014).
50. U. I. Kramm, J. Herranz, N. Larouche, T. M. Arruda, M. Lefèvre, F. Jaouen, P. Bogdanoff, S. Fiechter, I. Abs-Wurmbach, S. Mukerjee, J.-P. Dodelet, Structure of the catalytic sites in Fe/N/C-catalysts for  $\text{O}_2$ -reduction in PEM fuel cells. *Phys. Chem. Chem. Phys.* **14**, 11673–11688 (2012).
51. M. Ferrandon, A. J. Kropf, D. J. Myers, K. Artyushkova, U. Kramm, P. Bogdanoff, G. Wu, C. M. Johnston, P. Zelenay, Multitechnique characterization of a polyaniline-iron-carbon oxygen reduction catalyst. *J. Phys. Chem. C* **116**, 16001–16013 (2012).
52. J. S. Luo, J. L. Liu, Z. Y. Zeng, C. F. Ng, L. J. Ma, H. Zhang, J. Y. Lin, Z. X. Shen, H. J. Fan, Three-dimensional graphene foam supported  $\text{Fe}_3\text{O}_4$  lithium battery anodes with long cycle life and high rate capability. *Nano Lett.* **13**, 6136–6143 (2013).

**Funding:** This work is financially supported by 100 Talents Programme of Chinese Academy of Sciences, National Program on Key Basic Research Project of China (973 Program, grant nos. 2012CB215500 and 2014CB932300), National Natural Science Foundation of China (grant nos. 21422108, 21271168, 51472232, and 21471146), and The Jilin Province Science and Technology Development Program (grant nos. 20140101116JC and 20150520008JH). **Author contributions:** X.-B.Z. and Z.-L.W. developed the concept, designed the experiments, and wrote the manuscript. Z.-L.W., D.X., H.-X.Z., J.W., and F.-L.M. carried out the experiments. X.-B.Z., Z.-L.W., D.X., H.-X.Z., J.W., and F.-L.M. performed the analysis and wrote the manuscript.

Submitted 15 October 2014

Accepted 13 January 2015

Published 27 February 2015

10.1126/sciadv.1400035

**Citation:** Z.-L. Wang *et al.*, Gelatin-derived sustainable carbon-based functional materials for energy conversion and storage with controllability of structure and component. *Sci. Adv.* **1**, e1400035 (2015).

## Gelatin-derived sustainable carbon-based functional materials for energy conversion and storage with controllability of structure and component

Zhong-Li Wang, Dan Xu, Hai-Xia Zhong, Jun Wang, Fan-Lu Meng and Xin-Bo Zhang

*Sci Adv* 1 (1), e1400035.  
DOI: 10.1126/sciadv.1400035

ARTICLE TOOLS	<a href="http://advances.sciencemag.org/content/1/1/e1400035">http://advances.sciencemag.org/content/1/1/e1400035</a>
SUPPLEMENTARY MATERIALS	<a href="http://advances.sciencemag.org/content/suppl/2015/02/25/1.1.e1400035.DC1">http://advances.sciencemag.org/content/suppl/2015/02/25/1.1.e1400035.DC1</a>
REFERENCES	This article cites 51 articles, 2 of which you can access for free <a href="http://advances.sciencemag.org/content/1/1/e1400035#BIBL">http://advances.sciencemag.org/content/1/1/e1400035#BIBL</a>
PERMISSIONS	<a href="http://www.sciencemag.org/help/reprints-and-permissions">http://www.sciencemag.org/help/reprints-and-permissions</a>

Use of this article is subject to the [Terms of Service](#)

---

*Science Advances* (ISSN 2375-2548) is published by the American Association for the Advancement of Science, 1200 New York Avenue NW, Washington, DC 20005. The title *Science Advances* is a registered trademark of AAAS.

Copyright © 2015, The Authors